Magnetic, thermodynamic, and electrical transport properties of the noncentrosymmetric *B*20 germanides MnGe and CoGe

J. F. DiTusa,[1,*] S. B. Zhang,[2] K. Yamaura,[3] Y. Xiong,[1] J. C. Prestigiacomo,[1] B. W. Fulfer,[4] P. W. Adams,[1] M. I. Brickson,[5]
D. A. Browne,[1] C. Capan,[6] Z. Fisk,[7] and Julia Y. Chan[8]

[1]*Department of Physics and Astronomy, Louisiana State University, Baton Rouge, Louisiana 70803, USA*
[2]*International Center for Materials Nanoarchitectonics (MANA), National Institute for Materials Science, Tsukuba, Ibaraki 305-0044 Japan*
[3]*Superconducting Properties Unit, National Institute for Materials Science 1-1 Namiki, Tsukuba, 305-0044 Ibaraki, Japan*
[4]*Department of Chemistry, Louisiana State University, Baton Rouge, Louisiana 70803, USA*
[5]*Goshen College, Goshen, Indiana 46526, USA*
[6]*Department of Physics and Astronomy, Washington State University, Tri-City Campus, Pullman, Washington 99164, USA*
[7]*Department of Physics and Astronomy, University of California, Irvine, Irvine, California 92697, USA*
[8]*Department of Chemistry, University of Texas at Dallas, Richardson, Texas 75080, USA*

We present magnetization, specific heat, resistivity, and Hall effect measurements on the cubic *B*20 phase of MnGe and CoGe and compare to measurements of isostructural FeGe and electronic-structure calculations. In MnGe, we observe a transition to a magnetic state at $T_c = 275$ K as identified by a sharp peak in the ac magnetic susceptibility, as well as second phase transition at lower temperature that becomes apparent only at finite magnetic field. We discover two phase transitions in the specific heat at temperatures much below the Curie temperature, one of which we associate with changes to the magnetic structure. A magnetic field reduces the temperature of this transition which corresponds closely to the sharp peak observed in the ac susceptibility at fields above 5 kOe. The second of these transitions is not affected by the application of field and has no signature in the magnetic properties or our crystal-structure parameters. Transport measurements indicate that MnGe is metallic with a negative magnetoresistance similar to that seen in isostructural FeGe and MnSi. Hall effect measurements reveal a carrier concentration of about 0.5 carriers per formula unit, also similar to that found in FeGe and MnSi. CoGe is shown to be a low carrier density metal with a very small, nearly temperature-independent diamagnetic susceptibility.

I. INTRODUCTION

The silicides of Cr, Mn, Fe, and Co all which form in the *B*20 crystal structure type shown in Fig. 1, notable because of its lack of inversion symmetry, have been investigated for over 40 years yet continue to yield fascinating discoveries [1]. Although CrSi and CoSi appear to be simple paramagnetic (PM) metals [1], MnSi is helimagnetic (HM) below 30 K [2,3] and FeSi is a small band-gap insulator with unusual temperature- (*T*-) dependent properties [1,4–7]. Chemical substitutions among these materials, such as $Fe_{1-x}Mn_xSi$ and $Fe_{1-y}Co_ySi$, also display helimagnetism over wide regions of *x* and *y* as well as interesting behavior near the insulator-to-metal transitions for $x,y \sim 0.01$ [8–11]. The low symmetry of the *B*20 crystal structure gives rise to large Dzyaloshinskii-Moriya interactions causing long-period HM, rather than ferromagnetic (FM), ground states [12,13].

Investigations into the properties of MnSi have shown that the Curie temperature T_c is readily reduced by moderate pressure *P* with T_c approaching zero near 14 kbar [14]. Surprisingly, instead of accessing a quantum critical point with T_c going to zero, this system avoids criticality by undergoing a transition to an unusual state thought to be a crystal of topologically stable knots of the spin structure known as a skyrmion lattice [15–21]. There is also evidence for this unusual magnetic phase at ambient *P* over a small range of

magnetic field *H* and *T* near T_c, a region previously labeled as the *A* phase [17]. Evidence for a skyrmion lattice in thin samples $Fe_{1-y}Co_ySi$ and in FeGe exposed to small fields was discovered in Lorentz force microscopy images which observe a circulating magnetic moment on the length scale of the helimagnetic periods that exist at $H = 0$ [18,19].

In addition to these interesting magnetic properties, these materials may be important from a spintronics viewpoint [9]. Silicides are intrinsically compatible with silicon technologies and there are both insulating and metallic magnetic states with high carrier spin polarizations in this series. In addition, chemical substitutions between the monosilicides form easily and show little proclivity toward nucleating second phases. Thus, they may prove ideal for spin injection into silicon devices [9]. However, as the T_c's only reach 65 K for $Fe_{0.6}Co_{0.4}Si$ (see Fig. 2), they are not likely to be useful for most applications [1,8].

Given all of this interest, it is natural to ask if there are other isostructural materials that might also yield interesting magnetic ground states. Although CrGe is the only 3*d* TM germanide to have an equilibrium *B*20 crystal structure [25], FeGe crystallizes readily in this structure when the growth conditions are carefully controlled [27]. MnGe and CoGe are also known to form in this structure, but only under conditions of high pressure and temperature [28]. CrGe, much like chromium silicide, forms a nonmagnetic metal [25,29]. In contrast, FeGe has been the subject of much recent interest as it is very different from insulating FeSi displaying a metallic and HM ground state with a period of 70 nm and
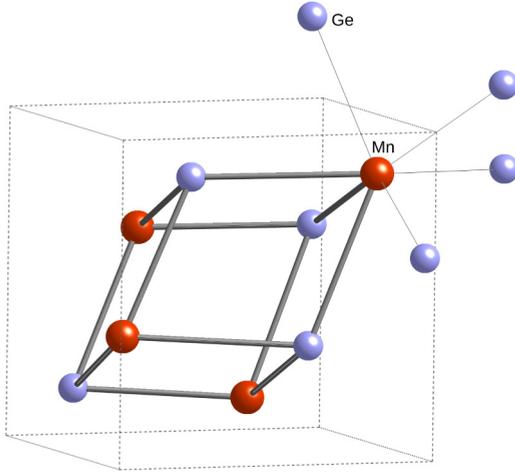
———
*ditusa@phys.lsu.edu

FIG. 1. (Color online) Crystal structure: Schematic of the cubic *B*20 crystal structure adopted by a number of the transition-metal (TM) germanide and silicide compounds including MnGe, MnSi, FeGe, FeSi, CoGe, and CoSi. The unit cell is indicated by the dotted lines. One of the important and interesting features of this structure evident in this figure is its lack of inversion symmetry. TM atoms occupy four sites that form a tetrahedron aligned along the (111) direction along with the four nonmetals positioned on a tetrahedron inverted relative to the TM atoms.

a $T_c = 280$ K [13,30,31]. The *A* phase of FeGe has recently been explored by Wilhelm *et al.* where they find a rich set of transitions that they suggest are due to symmetry changes stemming from solitonic intercore interactions and the onset of chiral modulations [32,33]. Electronic-structure calculations are interesting in that local density approximation (LDA), which correctly predicts a small band-gap insulating state for FeSi, predicts an even smaller band gap for the paramagnetic state for FeGe [34]. The metallic and magnetic ground state can be achieved by adding an onsite Coulomb repulsion (*U*) [34]. Thus, electronic-structure calculations confirm that FeGe is a metallic magnet and reveal that it has a nearly complete conduction electron spin polarization at low *T*. That FeGe has a T_c approaching room temperature, and hosts a skyrmion lattice phase for *T* just below T_c [19], suggests that there may be related materials with T_c's large enough to be considered for applications.

Here, we investigate the synthesis, magnetic, thermodynamic, and charge carrier transport properties of MnGe and CoGe to compare their properties to those found in the isostructural silicides with the goal of exploring the complex magnetic states of MnGe. We have included comparisons to calculations of their electronic structure and measurements of FeGe since the magnetic behavior of this compound is thought to be well established [13,32,33]. Previous investigations of MnGe reveal that it is very likely HM with a period that increases from 4 to 8 nm from 30 to 150 K with evidence that it hosts a skyrmion lattice over a wide range of *T* and *H* [24,35,36]. Although CoGe has properties similar to its periodic table neighbor CoSi [37], being a diamagnetic metal with a low carrier density, our data indicate that MnGe may be more complex than either MnSi or FeGe. Our ac and dc susceptibility data at low fields indicate a magnetic transition
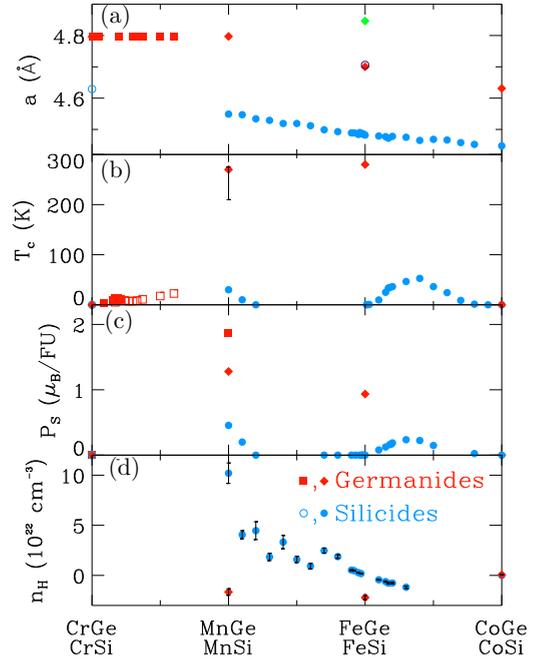

FIG. 2. (Color online) Phase diagram of the monogermanides and monosilicides having the *B*20 crystal structure: (a) Lattice constant *a*. Data for CrSi, open circle, from Ref. [22]. Green diamond is RuGe and violet circle is RuSi taken from Ref. [23]. (b) Curie temperature T_c (closed symbols), and spin-glass transition temperature (open symbols). Error bar drawn for MnGe demonstrates the difference in our data between T_c indicated in the low-field magnetic susceptibility and that obtained from a mean-field analysis of the high-field magnetization. (c) Saturation magnetization P_S as determined from the magnetization at high magnetic field. Filled square for MnGe indicates the value found in Ref. [24] at fields (150 kOe) not accessed in our experiments. (d) Carrier concentration n_H, determined from the ordinary Hall constant at 5 K for several germanide and silicide compounds identified on the *x* axis. Data for Mn through Co silicide taken from Ref. [9]. Data for $Cr_{1-x}Mn_xGe$ for $x \leqslant 0.6$ in frames (a)–(c), indicated with filled and open squares, taken from Refs. [25,26] with permission from the publisher.

at 275 K, while our magnetization data reveal a large saturated magnetic moment of >1.3 μ_B/f.u. Kanazawa *et al.* [24] have previously demonstrated that at low *T*, the magnetization saturates near 2 μ_B/f.u. at fields above those probed here. Several phase transitions are evidenced by sharp peaks in both our ac susceptibility and specific-heat data between 70 and 165 K that have not been previously observed. We suggest that these may be associated with the complex phase diagram expected in systems hosting skyrmion lattices as has been observed very near T_C in MnSi [38] and FeGe [32,33]. If this is true, the large *T* and *H* ranges where the skyrmion lattice state appears to be stable in MnGe [36] implies that it may be an ideal compound to explore these topologically interesting magnetic phases. A second phase transition at 120 K is also apparent in the specific heat that has no counterpart in the magnetic measurements and whose origin is still unknown. The transport properties of MnGe are very much like those of FeGe, but with a larger field scale consistent with the larger saturation field.

Our electronic-structure calculations for MnGe are largely consistent with the above description with a ferromagnetic ground state and a large carrier polarization energetically favored. Interestingly, a half-metallic state appears to be stable at a somewhat smaller lattice constant [39]. We present these results, along with the calculated Fermi surfaces, and compare the equilibrium lattice constant and reduced lattice constant solutions. Our results for CoGe indicate a very small carrier density metal with a correspondingly small Fermi surface (FS).

II. EXPERIMENTAL DETAILS

Polycrystalline samples of MnGe and CoGe were prepared from high-purity starting materials purchased from Wako Pure Chemical Industries, Ltd. and Rare Metallic Co. Ltd. The raw materials were checked for purity and the Ge powder was reduced in a 5% H_2 in Ar flow at 750 °C to remove any remaining oxide. These starting materials were ground into a fine powder and sealed in Ta/BN capsules. Samples were heated to 1200 °C for CoGe and 1300 °C for MnGe for a period of 1.5 h at a pressure of 6 GPa. Samples with excess Ge, $CoGe_{1.1}$, and $MnGe_{1.2}$ were grown under the same conditions in order to check the effect of any impurity phases on our results. X-ray powder diffraction data were obtained at room T using a Philips X'pert x-ray diffractometer with CuK_α radiation and confirmed using a Bruker Advance D8 powder diffractometer equipped with a focusing Ge(111) incident beam monochromator ($CuK\alpha_1$ radiation). CoGe samples showed no indication of any second phases and were determined to have the $B20$ crystal structure with a lattice constant a of 4.631 Å while $CoGe_{1.1}$ was also determined to have a $B20$ crystal structure with a larger lattice constant of 4.639 Å. MnGe samples displayed the same $B20$ crystal structure with $a = 4.797(4)$ Å. However, our powder diffraction patterns revealed the presence of a small amount second phase thought to be the high-temperature phase Mn_2Ge in our MnGe sample ($\sim$5%) with a larger fraction evident in our $MnGe_{1.2}$ sample ($\sim$20%). In addition, a small single crystal of MnGe was extracted from our sample and mounted on a glass fiber in a Nonius Kappa CCD diffractometer ($Mo K\alpha$, $\lambda = 0.71073$ Å) for single-crystal x-ray diffraction measurements. Refinement of the crystal structure using 107 reflections confirmed the $B20$ structure with a lattice constant of 4.797(4) Å. In the $B20$ structure (Wyckoff #198, $P213$), the atoms are at (u,u,u), $(1/2 - u, 1 - u, 1/2 + u)$, $(1 - u, 1/2 + u, 1/2 - u)$, and $(1/2 + u, 1/2 - u, 1 - u)$. Our refinement determined u to be 0.1377(2) for Mn and 0.84388(15) for Ge. Data were collected between 95 and 300 K that showed a thermal contraction of the lattice constant by $\sim$1% with cooling. The subtle crystal structure symmetry change at 170 K suggested in Ref. [35] was not observed although the consequences of this purported structural transition are near the limits of our ability to detect.

Single crystals of FeGe were grown by standard vapor transport techniques previously described in Refs. [27,31]. A stoichiometric mixture of high-purity elements were arc-melted and then placed in an evacuated quartz tube along with the transport agent, iodine. These were heated in a two-zone furnace for 1 week. Powder x-ray diffraction was employed to check the phase purity.

Magnetic susceptibility χ and magnetization M measurements were performed in a Quantum Design (QD) MPMSXL SQUID magnetometer in a 50-kOe superconducting magnet from 2.5 to 400 K. Both dc and ac susceptibility measurements were performed with the ac χ taken with an excitation fields of 1 Oe at a frequency of 30 Hz. Specific-heat measurements were performed in a QD PPMS using a standard semiadiabatic heat pulse technique from 2 to 300 K. The specific heat of MnGe was performed in fields of 0, 10, and 30 kOe provided by a superconducting magnet. Data presented here have been corrected by carefully subtracting the contribution from the measurement addenda. The electrical conductivity and Hall effect measurements on polycrystalline samples of MnGe and CoGe and single-crystalline samples of FeGe were performed on rectangular-shaped samples polished with emery paper. Thin Pt wires were attached to four Epotek silver epoxy contacts with an average spacing between the voltage probes of 0.5 mm. Samples had an average cross-sectional area of 1.0×0.1 mm^2. The resistivity, magnetoresistance, and Hall effect measurements were performed at 17 Hz using standard lock-in techniques in a gas flow cryostat and a 50-kOe superconducting magnet. Hall effect measurements were corrected for any misalignment of the leads by symmetrizing the data collected at positive and negative fields.

III. EXPERIMENTAL RESULTS

A. Magnetic susceptibility and magnetization

The dc χ of polycrystalline samples of both MnGe and CoGe are displayed in Fig. 3 along with χ of a single crystal of FeGe. The magnetic susceptibility of FeGe is quantitatively similar to that of previous measurements [31]. Measurements performed on the single crystal of MnGe separated from the same melt (without orientation) were nearly identical with those shown here for the polycrystalline sample. The general features of the magnetic susceptibility of MnGe that we
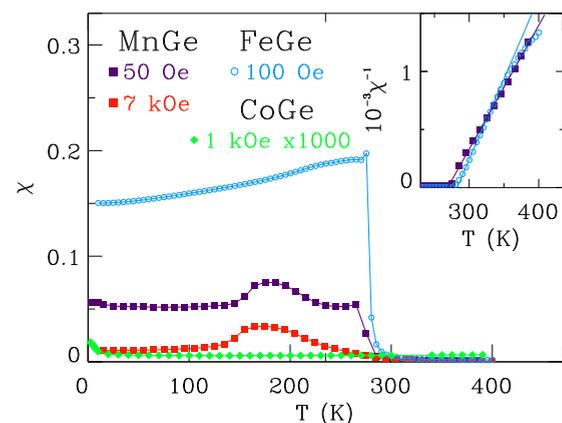
FIG. 3. (Color online) Magnetic susceptibility: dc magnetic susceptibility χ vs temperature T for FeGe, MnGe, and CoGe at magnetic fields indicated in the figure. Note that the CoGe data have been multiplied by a factor of 1000 for clarity. Inset: χ^{-1} vs T for FeGe and MnGe. Lines represent fits to Curie-Weiss behavior and correspond to Weiss temperatures of 284 and 270 K and magnetic moments of 1.0 and 1.35 μ_B per formula unit for FeGe and MnGe, respectively.
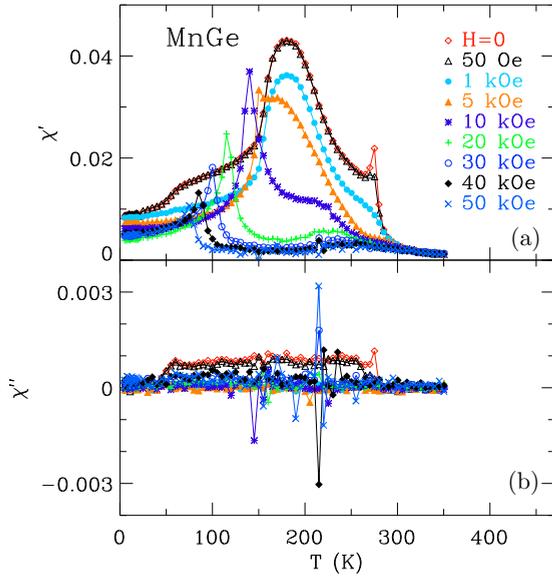
FIG. 4. (Color online) ac magnetic susceptibility: (a) Real χ' and (b) imaginary χ'' parts of the ac magnetic susceptibility vs T for MnGe at magnetic fields indicated in the figure. Lines connect the data points for display purposes.

FIG. 5. (Color online) Magnetization: Magnetic field H dependence of the magnetization M for MnGe at temperatures between 5 and 140 K (a) and between 150 and 400 K (b) as indicated in the figure. Lines connect the data points for display purposes. The hysteresis at low temperatures is apparent in the data at 5 K where both the initial increasing H magnetization (lower data) and the subsequent decreasing H sweep (upper data) are shown.

observe are similar to that measured previously [24], however, here we find a larger χ at low fields and a magnetic transition is observed near 275 K. We present χ of MnGe at 50 Oe and 7 kOe to display the variability with moderate fields that we observe. For temperatures above 290 K, Curie-Weiss behavior is apparent for both FeGe and MnGe as demonstrated in the inset. Here, the lines are fits of this form with a effective moment of 1.0 and 1.35 μ_B per formula unit (f.u.) and a Weiss temperature of 284 and 270 K for FeGe and MnGe, respectively. We have checked that these values are independent of H for $H \leqslant 50$ kOe for MnGe. The magnetic susceptibility of CoGe is paramagnetic, but much smaller, requiring an amplification by a factor of 1000 to make it visible on the scale of Fig. 3. A small upturn is seen below 20 K which is most likely due to a small density of paramagnetic impurities.

To explore more fully the subtle features apparent in our χ measurements of MnGe, we have measured the ac susceptibility over a wide range of T and H. The real part of the ac magnetic susceptibility χ' of MnGe is displayed in Fig. 4(a) and above 300 K yields a Weiss T and Curie constant within error of our dc results. We observe a sharp peak in the low field χ' at 275 K in agreement with the peak we observed in the low-field dc χ measurements. Below 250 K, a large increase in χ and χ' is followed by a broad maximum near 180 K. This broad peak is suppressed with field while a sharp peak in χ' becomes apparent at lower T for $H \geqslant 5$ kOe. These sharp features are indicative of a phase transition which moves to lower T with increasing H. The corresponding imaginary part of the ac susceptibility χ'' shown in Fig. 4(b) displays only a few features that can be considered as signal above the background. In particular, χ'' at fields 0 and 50 Oe is enhanced between 50 and 275 K which corresponds well to the region between the low-temperature shoulder and the sharp peak at
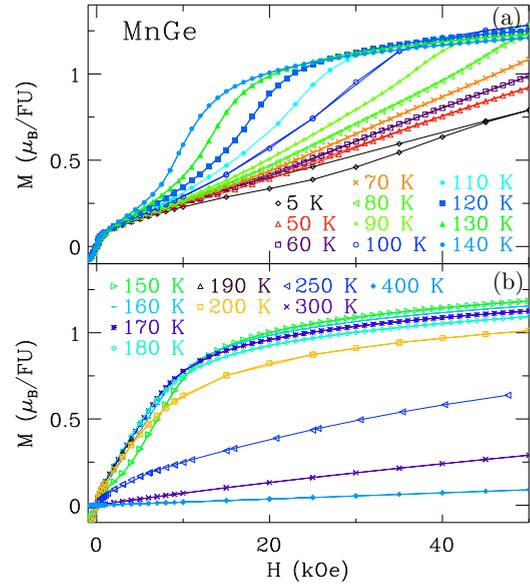
275 K in χ'. In addition, resonance features are apparent near 210 K for $H \geqslant 20$ kOe.

Equally as interesting is the evolution of the magnetization of MnGe in H and T as displayed in Fig. 5. Here, the linear $M(H)$ at 300 K and above confirms the PM state inferred from $\chi(T)$ while for $160 \leqslant T < 250$ K a large low-field contribution indicates a FM ordering with little hysteresis. These $M(H)$ curves are similar to that displayed by FeGe [30] as shown in Fig. 6 and MnSi [1] below T_c where a steep increasing $M(H)$ at low H is followed by a near saturation. However, MnGe requires about twice the field to reach an apparent saturation (~ 12 kOe) at these T's as compared to FeGe and MnSi. The small low-H hysteresis in $M(H)$ and the similarity of $M(H)$ with the other $B20$ compounds is consistent with, but not sufficient to determine, a HM ordered state in MnGe. We note that neutron diffraction measurements [24,35] have detected satellite peaks indicating a HM state in MnGe for $T < 170$ K.

In MnGe below $T = 150$ K, we observe an unusual suppression of $M(H)$ for $H > 1$ kOe with the saturation field moving to larger H as T is further decreased. These features are absent from the magnetization data for FeGe in Fig. 6. For MnGe at $T < 70$ K, we are not able to access the saturation field as it has moved well above our maximum field (50 kOe). We note that Kanazawa *et al.* have shown in Ref. [24] that the saturation magnetization approaches 2 μ_B/Mn at low temperatures and fields above 80 kOe. In addition to the increased saturation field at lower T, we observe a strong history dependence in the intermediate field range ($10 \leqslant H \leqslant 40$ kOe) as demonstrated at 5 K where we display both the initial up field sweep after cooling in zero magnetic
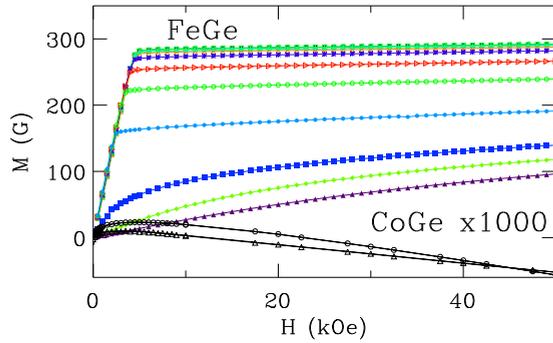
FIG. 6. (Color online) Magnetization of FeGe and CoGe: Magnetic field H dependence of the magnetization M for FeGe at temperatures of 2 K (black diamonds), 5 K (blue triangles), 10 K (green squares), 20 K (orange x's), 50 K (blue-green +'s), 100 K (blue *'s), 150 (red rightward-pointing triangles), 200 K (green circles), 250 K (light-blue bullets), 280 K (dark-blue filled squares), 290 K (light-green filled diamonds), and 300 K (violet filled triangles). The magnetization of CoGe multiplied by a factor of 1000 for clarity is also shown at temperatures of 5 (black circles) and 300 K (black triangles). Lines connect the data points for display purposes.

field and the subsequent downward H sweep. This hysteresis is similar to what is measured in MnSi and FeGe for fields between 1 and 6 kOe. Figure 7 displays the field dependence of χ' demonstrating the structure and sharp transitions that occur with field. In particular, the very sharp peak in the 100-K data near 30 kOe, as well as the broader peak in the 150-K data below 10 kOe, correlate well with the sharp maxima found in the T dependence of Fig. 4(a). These features occur at fields a few kOe below the fields where M begins to saturate. It is interesting to note that detailed investigations of the ac susceptibility of both MnSi and FeGe reveal a rich field dependence that is restricted to temperatures near the Curie point. These have been shown to be associated with the transitions into, and out of, the A phase that has been associated with a skyrmion lattice state. In our MnGe data, we observe a somewhat different structure in $\chi'(H)$ over a much wider T range and at larger H.

The $M(H)$ for CoGe in Fig. 6 shows a small diamagnetic high-field contribution, which may indicate that the intrinsic
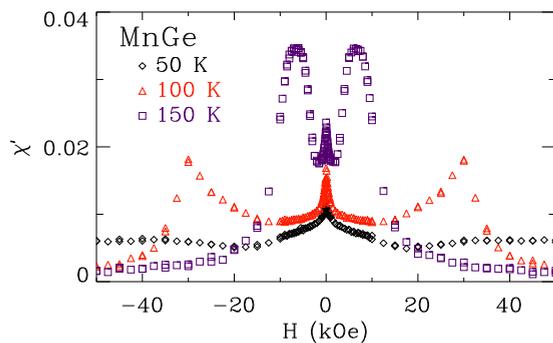

FIG. 7. (Color online) Field dependence of the ac susceptibility: The real part of the ac susceptibility χ' of MnGe at three temperatures demonstrating the rich structure and sharp transitions that occur with field H below the Curie temperature.
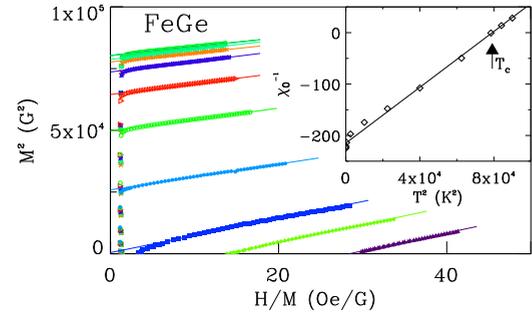

FIG. 8. (Color online) Arrott plot for FeGe: The square of the magnetization M^2 plotted vs the ratio of the magnetic field H to M to compare with a standard mean-field form of M commonly known as an Arrott plot [40]. Symbols are the same as in Fig. 6. Solid lines are linear fits to the high-field behavior. Inset: plot of the H/M intercepts χ_0^{-1} of linear fits in the main frame to determine the Curie temperature T_c as indicated in the figure.

behavior of CoGe is diamagnetic and that the low-field paramagnetic contribution may be extrinsic. Similar to the T dependence of χ in Fig. 3, we observe only minor T dependence to the magnetization of CoGe. We do not observe any features similar to that reported by Ref. [28] in our CoGe samples and find no indication of an antiferromagnetic transition near 120 K.

To begin to establish a magnetic phase diagram for MnGe, and to compare directly with FeGe we have performed a standard mean-field analysis to our $M(H,T)$ data commonly known as an Arrott plot [40] as demonstrated in Figs. 8 and 9. It is apparent from the linearity of M^2 as a function of H/M at high fields that FeGe is well described in terms of a simple mean-field treatment. In addition, the Curie temperature T_c determined by finding the temperature where our high-field linear fits intercept the origin, agrees well with T_c indicated by the peak in $\chi(T)$ and with θ_W. In contrast, the Arrott plots for MnGe (Fig. 9) are not as simple to interpret. We observe a change from a positive intercept of the H/M axis (χ_0^{-1}) for $T \geqslant 250$ K to a negative intercept at $T \leqslant 200$ K indicating that T_c lies between these two temperatures. We locate the transition further by plotting χ_0^{-1} versus T^2 displayed in the inset to Fig. 9(a) as suggested by the Stoner-Edwards-Wohlfarth model for weak itinerant ferromagnets [41]. The plot indicates that χ_0^{-1} goes to zero at 220 ± 10 K. This is in contrast to both the peak in $\chi(T)$ and $\chi'(T)$, and θ_W for MnGe which are consistent with a magnetic transition T near 275 K. However, as demonstrated in the inset to Fig. 9(b), both $d\chi/dT$ and $d\chi'/dT$ display a minimum at 210 K. Furthermore, $\chi''(T)$ shown in Fig. 4(b) displays a strong signal near 210 K at fields above 20 kOe consistent with this critical temperature determination. A more detailed modified Arrott analysis was carried out to determine the variation of the critical temperature with the choice of critical exponents. We found a variation of T_c of no more than 20 K for a wide range of exponents. Thus, we have observed an inconsistency in the low-field behavior indicating a magnetic transition at 275 K and a standard Arrott analysis of the magnetization above 20 kOe where our fits to the mean-field form are performed. We note that a previous investigation of MnGe has reported a T_c of 170 K [24], well
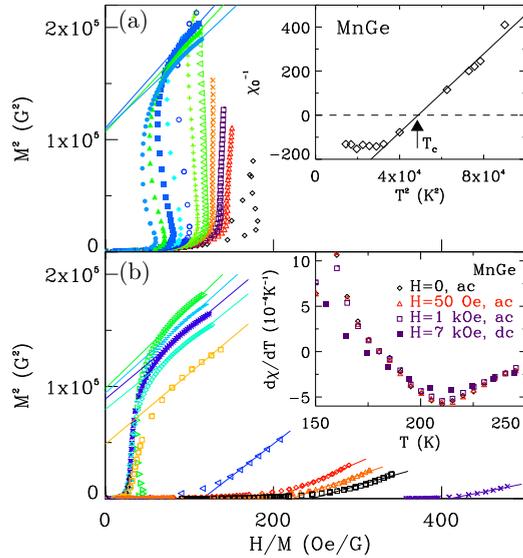
FIG. 9. (Color online) Arrott plots for MnGe: (a), (b) The square of the magnetization M^2 plotted vs the ratio of the magnetic field H to M [40]. Symbols are the same as in Fig. 5 with the addition of data at 270 K (red diamonds), 275 K (orange triangles), and 280 K (black squares) in frame (b). Solid lines are linear fits to the high-field behavior. Inset to frame (a): plot of the H/M intercepts χ_0^{-1} of linear fits in the main frame to determine the Curie temperature T_c as indicated in the figure. Inset to frame (b): derivative of the magnetic susceptibility χ and χ' shown in Figs. 3 and 4, with respect to temperature T vs T. The minimum in $d\chi/dT$ corresponds closely to T_c determined from the Arrott analysis in the inset to (a).

below either of these transition temperatures observed in our data.

The data presented here, including our χ' measurements of Figs. 4(a) and 7, and our $M(H)$ curves below 150 K, suggest that the steep increase in $M(H)$ that we observe at intermediate temperatures and fields may indeed be a thermodynamic phase transition rather than a simple crossover between two simply related magnetic states of MnGe. The wide-field range required for saturation of M which increases upon cooling is clearly distinct from that seen in FeGe and MnSi [1,30]. We note that in this T range, Refs. [24,36] report a significant decrease in the HM period consistent with a larger saturation field. The steep increase in $M(H)$ and the corresponding sharp peak in χ' that we observe is interpreted as a phase transition just below the field necessary to induce a ferromagnetically aligned state. As such, this phase transition may be associated with a change from the A phase, where a skyrmion lattice is expected, and a conical or a field-induced FM phase as occurs only in a small-T region below T_c in MnSi, FeGe, and $Fe_{1-x}Co_xSi$.

Our $MnGe_{1.2}$ samples displayed a χ and M that reproduced all of the essential features outlined for MnGe above. However, the low field ($H \leqslant 1$ kOe) M was enhanced beyond that of MnGe by almost a factor of 2 for $T < 275$ K, while the 50-kOe results were within error of each other. In addition, like our CoGe sample, our $CoGe_{1.1}$ sample displayed a small, T independent χ of 6×10^{-6} from 400 down to 50 K with a Curie tail apparent at low T. The Curie-type behavior observed
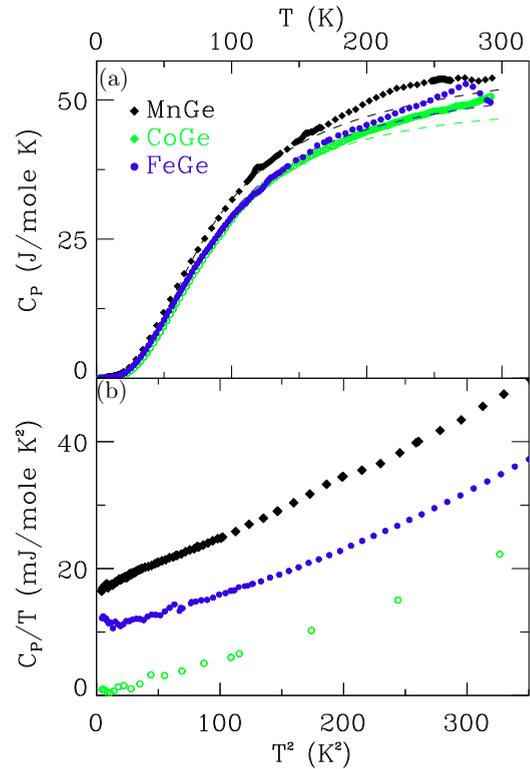

FIG. 10. (Color online) Specific heat: (a) Specific heat C_P vs temperature T of MnGe, FeGe, and CoGe at zero field. Dashed lines are fits of a model for the phonon contribution to $C(T)$ that includes Debye and Einstein terms. (b) C_P/T vs T^2 at zero field and low temperatures.

below 20 K is consistent with a spin-$\frac{1}{2}$ impurity concentration of 1%.

B. Specific heat

The specific heat C_P at $H = 0$ of MnGe, CoGe, and FeGe is plotted in Fig. 10(a) for $2.0 \leqslant T \leqslant 300$ K. Small peaks at 119, 160, and 165 K as well as significant structure above 200 K are apparent in the MnGe data. In order to parametrize these data, we have fit the Debye model with Einstein terms added to represent the optical phonon contribution to our data [42]. This model with Debye temperatures of 272, 269, and 281 K and characteristic T of 324, 282, and 319 K for the optical branches for FeGe, MnGe, and CoGe, respectively, represents the data fairly well. A clear deviation of the model from the data can be seen at high temperatures for all three compounds as well as the peak structures noted above for MnGe and the peak at the Curie temperature of FeGe. Figure 10(b) of the figure shows C_P/T plotted as a function of T^2 in the usual manner for displaying the electronic and spin-wave contributions to C_P. Here, it is apparent that the linear-in-T terms are quite different for the three compounds with coefficients γ of 16, 9 [31,43], and ~ 0 mJ/mole K^2 for MnGe, FeGe, and CoGe, respectively. γ of MnGe and FeGe are comparable to that found in MnSi (32 mJ/mole K^2) [38].

In Figs. 11(a) and 11(b), we plot C_P/T after subtracting the model represented by the dashed lines in Fig. 10(a) in order to highlight the more subtle features of C_P/T. C_P/T for MnGe is
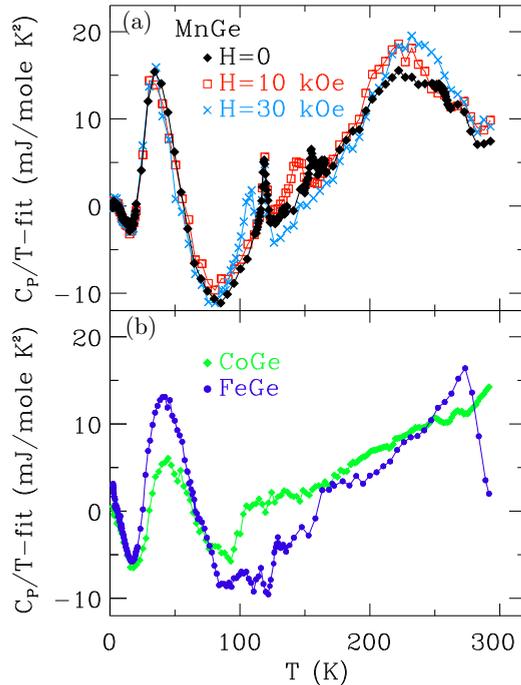
FIG. 11. (Color online) Specific heat after subtraction of a model for the phonon contributions: (a) C_P/T of MnGe at fields identified in the figure after subtraction of the model represented by the dashed line in Fig. 10(a) vs T. Several phase transitions are apparent. (b) C_P/T vs T^2 for FeGe and CoGe at zero field after subtraction of the model represented by the dashed lines in Fig. 10(a). Lines connect the data points for display purposes.

plotted for fields of 0, 10, and 30 kOe in Fig. 11(a) to display its field dependence. We observe several features that these data have in common for the three materials, including a broad maximum near 50 K that we attribute to phonon contributions that are not reproduced by our simple model. In addition, there are several features that are apparent in the MnGe and FeGe data that do not appear in our CoGe data. For FeGe, we observe a sharp peak in $C_P(T)$ at the Curie temperature which is similar to that measured in Ref. [32]. The specific heat of MnGe appears to be far more interesting, displaying several distinct peaks and a broad region above 200 K with a magnitude that exceeds our simple model of the phonon contribution by $\sim$10 mJ/mol K^2. However, no distinct sign of a phase transition near 275 K is visible in our data. Perhaps more interesting are the three sharp peaks in the $H = 0$ data of MnGe, one at 119 K and a pair at 160 and 165 K, close to the magnetic transition temperature identified in Ref. [24]. Application of a magnetic field of up to 30 kOe has no effect on the temperature or shape of the peak we observe at 119 K. In contrast, we observe a steep decrease in the peak T of the 160-K feature with H so that a single peak is observed at 145 K in 10 kOe and at 110 K at 30 kOe. Thus, by 30 kOe the field-dependent peak occurs at lower T than the field-independent $T = 119$ K feature.

The field-dependent phase transition identified here corresponds closely in T and H with the peaks we observed in χ' in Fig. 4 and dM/dH determined from the data in Fig. 5 and which we associate with a phase transition that
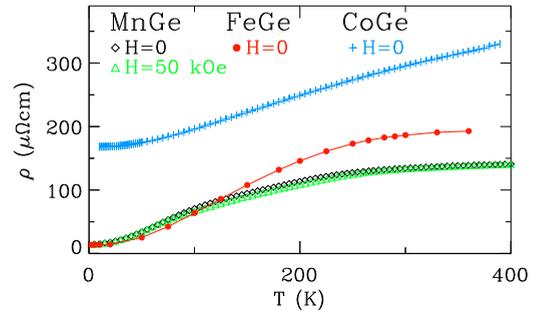

FIG. 12. (Color online) Resistivity: Resistivity ρ vs temperature T at fields H identified in the figure for FeGe, MnGe, and CoGe.

occurs at several kOe below the field needed to induce a FM state. In contrast, we see no indication in any of the magnetic measurements for a phase transition at 119 K, which, when considered along with the observation that this transition is not field dependent, suggests that this transition may not be related to the magnetic state of the system. It is somewhat difficult to reconcile a phase transition in either the structure or electronic properties of this itinerant magnet that has no effect on the magnetic properties. As we noted above, we have measured the single-crystal x-ray diffraction of a small crystal separated from the melt at T's down to 95 K in order to search for structural changes that may be the cause of the 119-K phase transition. We found no differences in the x-ray data outside of a 1% thermal contraction of the lattice when compared to our room-T results. It remains possible that there is a more subtle structural transition that we are not sensitive to in our single-crystal x-ray diffraction experiments such as the tetragonal distortion suggested in Ref. [35]. Thus far, we have not identified the cause of the phase transition apparent in C_P at 119 K in our MnGe sample.

C. Resistivity

The resistivities of FeGe, MnGe, and CoGe displayed in Fig. 12 are that of metals with residual resistivity ratios RRR = $\rho(300 \text{ K})/\rho(4 \text{ K})$, of 14, 9.3, and 1.8 for FeGe, MnGe, and CoGe, respectively. The corresponding residual resistivities $\rho(4 \text{ K})$ are 13.5, 15.5, and 160 $\mu\Omega$ cm. There are no obvious features in the T dependence of ρ that correspond to either T_c's of FeGe and MnGe nor the phase transition identified in $C(T)$ at lower T for MnGe. Below 10 K, a T^2 dependence of $\rho(T)$ becomes apparent in FeGe and MnGe with coefficients $A = 0.8$ and 9.2 nΩ cm/K^2. These values can be compared to that measured in MnSi which is about three times larger than our value for MnGe [44,45]. It is interesting to note that for these compounds FeGe, MnGe, and MnSi, the ratio A/γ^2 is between 1×10^{-5} and 3.0×10^{-5} $\mu\Omega$ cm (mole K/mJ)^2 or about one to three times the value reported by Kadowaki and Woods for heavy-fermion metals [38,46]. In MnGe, the application of a 50-kOe field reduces ρ by a few percent over most of the T range covered, suggesting that the field reduces the magnetic fluctuation scattering of the carriers.

A more detailed view of the magnetoresistance (MR) of all three compounds is shown in Figs. 13(a) and 13(b) where the field dependence is displayed. For both MnGe and FeGe, a negative $\Delta\rho/\rho_0$, where $\Delta\rho = \rho(H) - \rho_0$ and ρ_0 is the
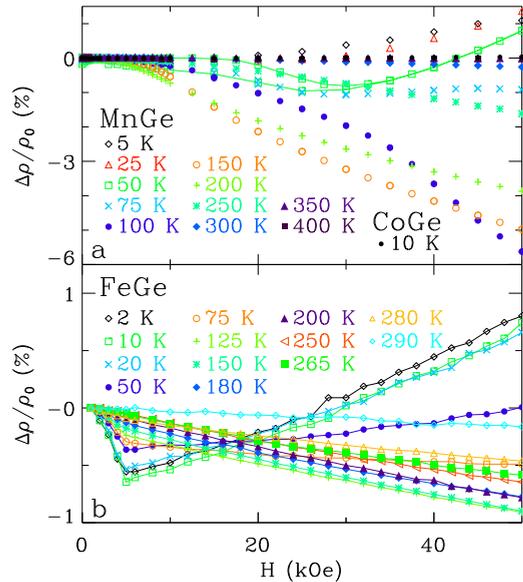
FIG. 13. (Color online) Magnetoresistance: (a) Magnetoresistance $\Delta\rho/\rho_0 = [\rho(H) - \rho_0]/\rho_0$, where ρ_0 is the zero-field resistivity, of MnGe and CoGe at temperatures indicated in the figure. The hysteresis at low temperatures is demonstrated by the 50-K data where both the increasing and decreasing field data are shown. (b) $\Delta\rho/\rho_0$ for FeGe at temperatures indicated in the figure. Lines connect the data points for display purposes.

zero-field resistivity, reaches its largest absolute value near 100 K. At lower T, a positive MR contribution is observed that grows with reduced T. In FeGe, a distinct change in the MR occurs at the transition to the field-induced FM state near 6 kOe. A similar, yet less obvious, change is visible in the MR of MnGe along with a hysteretic behavior associated with the transition to the FM phase and which is maximized near 50 K. We demonstrate the hysteric MR in the figure by displaying both the increasing and decreasing field data at 50 K. This hysteresis occurs in the same field range as the hysteresis identified in $M(H)$ in Fig. 5. These features of the MR of MnGe and FeGe are similar to those observed in MnSi as all three display a negative MR with sharp changes observed near the crossover to field-induced ferromagnetism. However, in MnSi the negative MR near $T_c = 30$ K can be as large as -40% for clean samples (see Ref. [47] for example). The obvious hysteresis demonstrated in the figure for MnGe appears to be unique to this compound. In all three of these materials, the positive contribution to the MR dominates at $T < 5$ K. The MR of CoGe is very small and positive, being less than 0.1% at 10 K and 50 kOe (Fig. 13).

The carrier densities of all three compounds have been estimated from the high-field Hall effect. A detailed presentation of the Hall data including the anomalous Hall effect [24] will be presented elsewhere [44]. Here, we report the carrier densities implied by the simplest interpretation of the Hall constant $R_0 = 1/nec$ as presented in Fig. 2(d). While MnGe and FeGe have metallic carrier densities consistent with about $\frac{1}{2}$ to $\frac{2}{3}$ carrier per formula unit, CoGe has a much smaller carrier density, rising with T from 0.6 to 1.3×10^{21} cm^{-3}. Thus, while MnGe and CoGe appear to be very similar to their

silicide counterparts, MnSi and CoSi, in their magnetic and electronic states, FeGe is well known to be very different from the nonmagnetic insulator FeSi [31].

IV. ELECTRONIC-STRUCTURE CALCULATIONS

In order to better determine where electronic interactions are significant in the transition-metal (TM) germanides with the $B20$ crystal structure and to compare their relative importance, we calculate the electronic properties of MnGe, FeGe, and CoGe using a standard density functional approach. The $B20$ structure is a cubic structure with a rather low internal symmetry, as demonstrated in Fig. 1, so that there is neither fourfold rotation symmetry nor inversion symmetry in the lattice. This low symmetry is thought to be responsible for the interesting magnetic properties of materials having this structure as outlined in the Introduction. Although the effects of the low symmetry, as reflected in the importance of spin-orbit coupling, for example, may be restricted to energy scales too small to be captured in our models, our calculations are useful in that they provide a starting point for understanding what role spin-orbit splitting may play. Similarly, this method is a clear approximation in terms of the electron interactions in the strongly localized d orbitals. However, we believe that it provides a very useful first approximation to understanding the role the interactions play. By comparing these results with experiment, we can identify where the electronic interactions and spin-orbit splitting of the bands are significant and where they play a minor role. We also investigate these materials in a variety of conditions, varying the lattice constant as might be accomplished with alloying to examine the possible ground states and to compare to the experimental results presented here.

We use the standard WIEN2K all-electron density functional theory (DFT) package [48] that uses a linearized augmented plane-wave (LAPW) basis including local orbitals. We have chosen for our study to use the generalized gradient approximation (GGA) functional [49], which provides a significant improvement over LDA in terms of bond lengths and other properties. It is also considered to be a good choice for systems of moderate interaction. For the calculation of MnGe, we chose muffin-tin radii of 2.34 a.u. for Mn and 2.23 a.u. for Ge. For FeGe, the TM and Ge radii were 2.28 and 2.17 a.u., and for CoGe they were 2.31 and 2.23 a.u. For MnGe, we used $u = 0.135$ and 0.842, for FeGe we used $u = 0.130$ and 0.839, and for CoGe we used $u = 0.140$ and 0.841. These values are close to the experimental positions; in our calculations we found the residual forces at these positions to be less than 0.03 Ryd/a.u. In the calculations, the plane-wave cutoff $R * K_{\max}$ was varied from 7.0 to 9.0 to ensure the basis set and energies had converged. For most of the calculations, we employed a grid of $19 \times 19 \times 19$ k points for Brillouin zone (BZ) integrations (340 in the irreducible zone). For FS calculations, we used a denser $34 \times 34 \times 34$ grid. We used the modified tetrahedron method [50] to perform integrals over the Brillouin zone. While the observed ground state of MnGe and FeGe is helimagnetic, the pitch of the helical order is much larger than the unit-cell size, so we have done our magnetic calculations assuming a uniform ferromagnetic state.

In Fig. 14, we show the total energy and total magnetic moment of MnGe in possible magnetic (2) and nonmagnetic
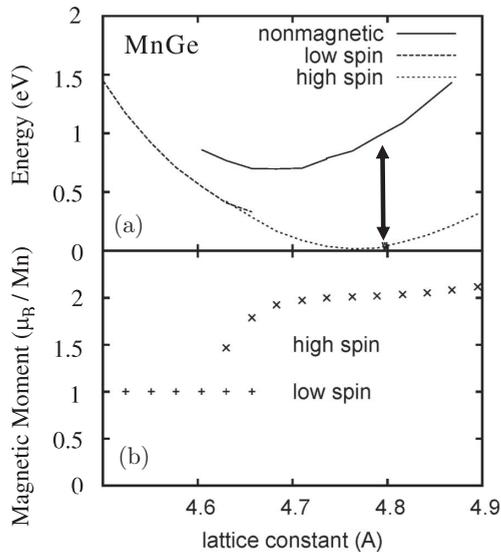
FIG. 14. Total energy and magnetic moment of MnGe: (a) Total energy per unit cell variation as a function of MnGe lattice constant. Arrow indicates the experimental lattice constant. (b) Magnetic moment per Mn atom calculated as a function of lattice constant.
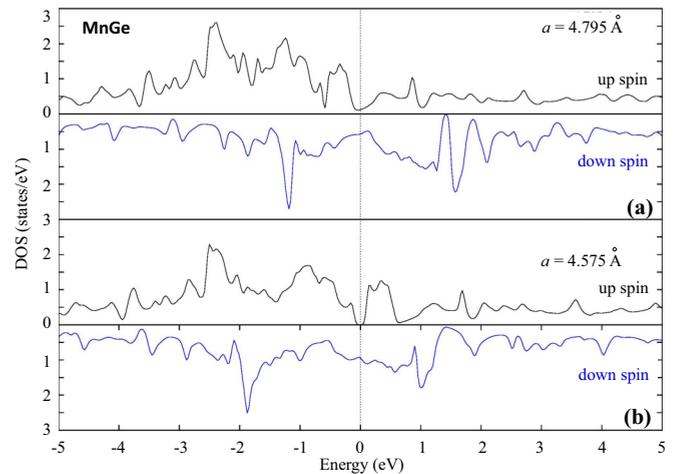

FIG. 15. (Color online) DOS for MnGe for two different lattice spacings: Density of states (DOS) for both the majority (spin-up) and minority (spin-down) subbands calculated at the experimental lattice constant (a) and at a smaller lattice constant (b).

ground states for a range of lattice constants. We find that a magnetic ground state is preferred at the experimental lattice constant, and remains that way until the lattice constant is reduced to 4.46 Å (not shown). There appear to be two competing magnetic ground states in MnGe with Fig. 14(b) showing that the predicted moment is close to 2 μ_B/Mn at the experimental lattice constant and that the moment abruptly collapses to 1 μ_B/Mn at about 4.6 Å similar to what was predicted in Ref. [39]. This drastic change in the electronic structure suggests measurements of the magnetic moment and magnetic ordering under applied pressure such as that recently carried out by Deutsch *et al.* [51]. The calculated bulk modulus of MnGe is 238 GPa so that a characteristic pressure for the transition is predicted to be close to 28 GPa suggesting diamond anvil techniques may be required to access this transition. However, in Ref. [51] this transition was found to occur at a much smaller pressure, near 6 GPa. Interestingly, the chiral order was found to persist at pressure above the transition, but with a reduced helical pitch.

The nature of the rapid collapse of the magnetic moment with reduction of the lattice constant can be clearly seen in the DOS of MnGe presented for two lattice spacings (4.795 Å, high-moment solution) and (4.575 Å, low-moment solution), shown in Fig. 15. The 2 μ_B/Mn state has both spin-up and -down carriers present at the Fermi energy, but the low-moment state seen at small lattice constant is a half-metallic state with only minority-spin carriers present at the Fermi level [39]. The predominant change is that the peak in the spin-up DOS lying between −0.5 and 0 eV for the high-moment solution [Fig. 15(a)] has moved upward in energy so that the gap visible near −0.5 eV in Fig. 15(a) moves to the Fermi level in the low-spin solution shown in Fig. 15(b). This change corresponds to two complete bands shifting from just below the Fermi energy to just above the Fermi energy. Hence, we conclude that under pressure, MnGe should become half-metallic and

suffer a rapid drop in total moment. It is interesting to note that in Fig. 5 $M(H)$ tends to saturate at high T at $M \sim 1.25$ μ_B/Mn whereas at low T, $M(H)$ tends to saturate near 2 μ_B/Mn [24]. The mechanism for this variation with T is unknown, and our calculations do not explain why this change occurs for such a small increase in T. We speculate, however, that the variation in the saturated magnetization with T may be related to the competition between these two ground states that lie close in total energy.

In all of these B20 materials, including the silicides, the states within 5 eV of the Fermi energy are predominantly derived from the TM d orbitals, and it is believed they drive much of the interesting properties of these compounds. To highlight the changes to the DOS with filling of the d orbitals across the series, and to place our MnGe results in context, we show in Fig. 16 the total DOS for MnGe, FeGe, and CoGe. What is most striking about this figure is the similarity of the DOS in the majority-spin bands of MnGe and FeGe to the DOS of CoGe. In fact, the shape of the density of states is similar across this series with the main difference being the placement of the Fermi level. One remarkable feature made clear by this plot is the appearance of a pair of gaps (or in some cases deep minima) in the DOS within about 2 eV of the Fermi level. The gap that appears at roughly 0.5 eV lower in energy is responsible for the well-studied insulating behavior of FeSi and where the large DOS seen at the gap edges is thought to be important in creating many of its interesting temperature- and doping-dependent features. These features, resulting from d-band splitting by the low symmetry of the crystal field, are seen in almost all DOS of these TM silicides and germanides [37,52–56]. We note that a magnetic ground state for FeGe is found with a magnetic moment near 1 μ_B in agreement with prior calculations and experiments [30,34,52,53]. This is in contrast to our calculations for CoGe in which the energy minimization converges to nonmagnetic state for all lattice constants probed [37]. The defining feature of the DOS of CoGe is the pseudogap residing close to the Fermi level in a similar fashion to the majority-band case of both MnGe and
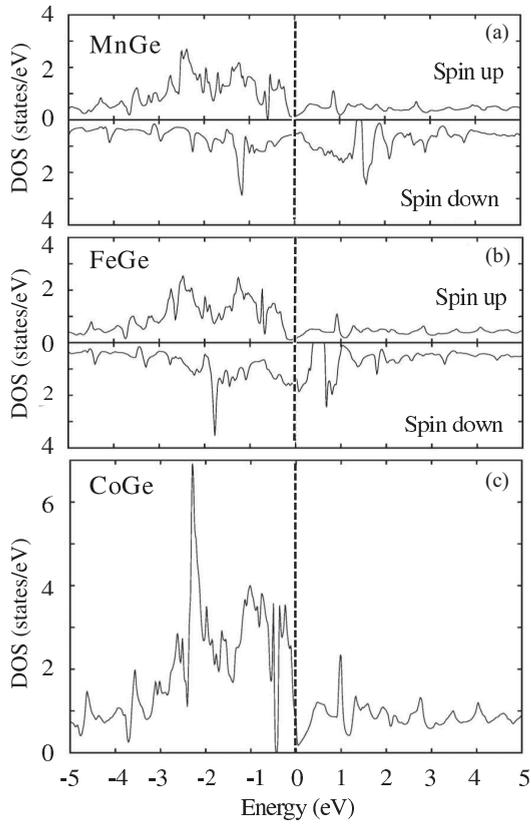
FIG. 16. DOS for MnGe, FeGe, and CoGe: Density of states (DOS) for both the majority (spin-up) and minority (spin-down) subbands of MnGe and FeGe, as well as the DOS of CoGe calculated at the experimental lattice constants.

FeGe as well as to the case of CoSi [55]. This placement of the Fermi energy reduces the DOS at the Fermi level for CoGe to about 1 state per eV per unit cell. The paramagnetic ground state of CoGe may very well be a result of a smaller DOS at the Fermi level as compared to either the itinerant magnets FeGe or MnGe. That the Fermi level lies in a deep valley in the DOS also correlates well with the small apparent charge

FIG. 18. (Color) Band structure of majority (spin-up) and minority (spin-down) spin subbands of FeGe: Energy bands calculated at points of high symmetry at the experimental lattice constant.

carrier concentration, about 0.04 charge carriers per CoGe formula unit, determined from the Hall voltage.

The similarity in the DOS of the three materials suggests that the band structure can be well understood from a rigid band approximation where only the electron count and the splitting of the Fermi energy in the spin subbands account for the changes. This can be seen in Figs. 17–19, where the results of our band-structure calculations are presented. For MnGe (Fig. 17) and FeGe (Fig. 18), the band structure is shown for both spin orientations and the identity of each of the bands is indicated by its color so that they can be traced across each of the three figures. Again, we draw attention to the similarity of the electronic structure of CoGe with the majority-spin bands in MnGe and FeGe. In each case, the Fermi level lies near the top of a set of two bands, identified by their black and gold colors, and at the bottom of second pair of bands which are green and gray. In addition, there appears to be a Dirac point
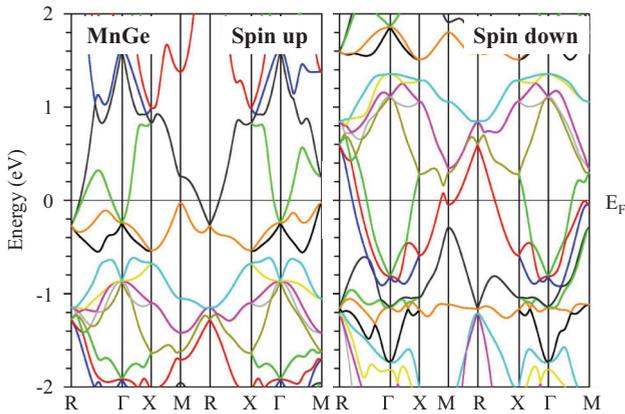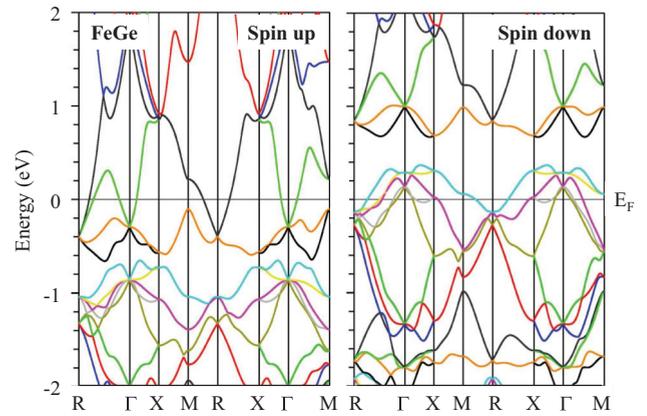

FIG. 17. (Color) Band structure of the majority (spin-up) and minority (spin-down) subbands of MnGe: Energy bands calculated at points of high symmetry at the equilibrium lattice constant.
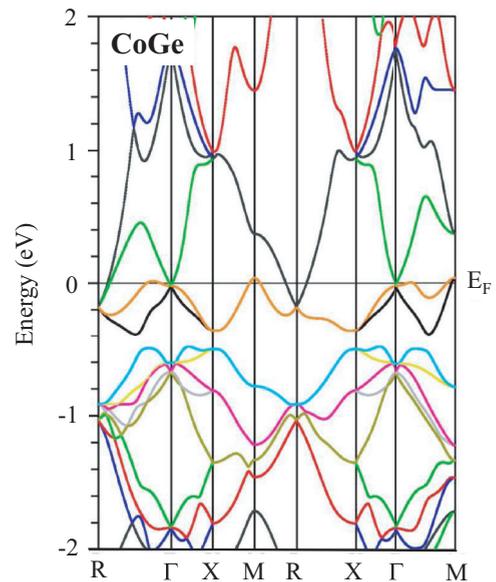

FIG. 19. (Color) Band structure of CoGe: Energy bands calculated at points of high symmetry.
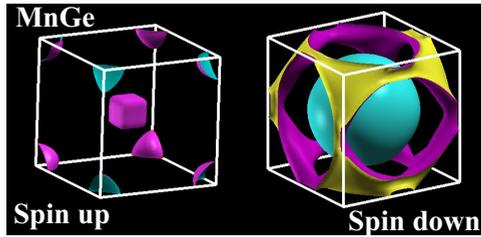
FIG. 20. (Color online) Fermi surface of MnGe: The majority-spin subbands (spin up) are displayed on the left and minority-spin subbands (spin down) are shown on the right.

FIG. 22. (Color online) Fermi surface of CoGe.

in the electronic structure of CoGe at the Γ point, however, the consequences of this unusual structure are likely masked by the larger population of charge carriers associated with bands crossing the Fermi energy at different k points within the BZ [37]. A comparison to the band structure of the silicides reveals many similarities with the largest difference coming from the 30% reduction in bandwidth of the germanides resulting from the ∼5% increase in lattice constants (see Fig. 2). As a result, the relative shift of the spin subbands in MnGe and FeGe are larger than their silicide relatives, leading to the larger magnetic moments found in the germanides.

Finally, we present plots of the Fermi surfaces of MnGe in Fig. 20, FeGe in Fig. 21, and CoGe in Fig. 22. This comparison highlights both the similarities in the majority-spin subbands of MnGe and FeGe with the electronic structure of CoGe, as pointed out earlier, and the dominance of the carriers in the spin-minority bands of MnGe and FeGe. This last point is made clear by the small pockets of FS in the spin-up bands of MnGe and FeGe as compared to the respective spin-down bands. The small FS sheets in these subbands reflect the tendency for the spin-up FS, along with the single FS in CoGe, to lie near the same minimum in the DOS demonstrated in Fig. 16. Thus, these Fermi surfaces consist of a small pocket of electrons near Γ or, in the case of CoGe, a Dirac point represented by the small red sphere at the center of Fig. 22, and two
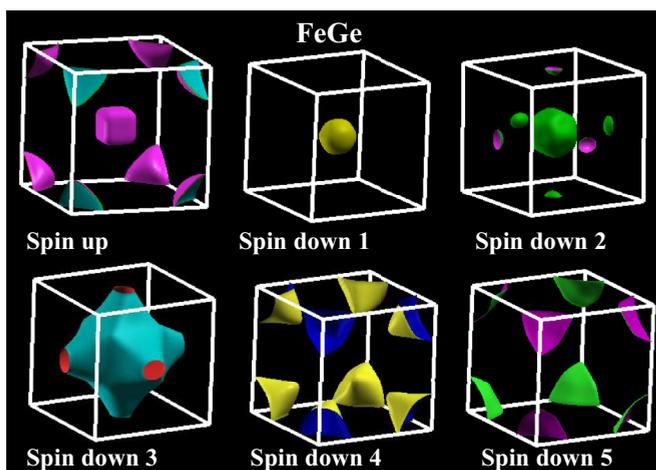

FIG. 21. (Color online) Fermi surface of FeGe: The majority-spin subbands (spin up) are shown in the top left frame and the five minority-spin subbands (spin down) are displayed in remaining frames.
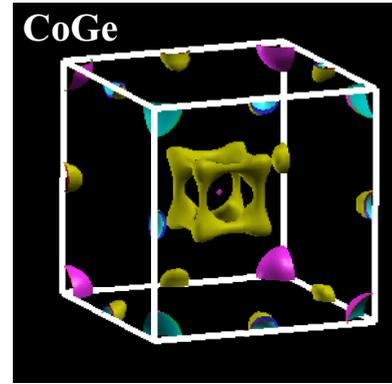
pockets of electrons at the R point (corner of the BZ shown in the figures). These pockets are not very spherical, having a significant octahedral distortion, which is not surprising given the low site symmetry in this structure. In the case of CoGe, there are also two small crosslike features of holes centered at the M point and a cagelike structure centered on Γ that is associated with a band that crosses the Fermi level (holes) by only a few meV which is below the uncertainty inherent in our calculations. Thus, the existence of this FS sheet is in question. We have checked this result by including spin-orbit coupling in our calculation of the electronic band structure of CoGe to better determine which of the small number of bands at the Fermi level cross, finding no discernible differences. This is in contrast to the much larger and, in the case of FeGe, more numerous FS sheets in the minority-spin bands of MnGe and FeGe consistent with the large ordered magnetic moment we measure for both of these below T_c.

There are several aspects to these FS sheets that reflect the low symmetry of the $P2_13$ space group including the elliptical, rather than circular, shape of the intersection of the spin-down FS sheets of MnGe and FeGe with the BZ boundary. This is a direct consequence of the lack of fourfold rotational symmetry in the B20 structure. Notice that the orientation of these ellipses rotate by 90° on neighboring faces of the cubic BZ. In addition, as has been pointed out for the FS of MnSi [56], the FS sheets do not always intersect the BZ boundary at right angles. As Jeong points out for MnSi [56], the periodicity of the FS relies instead on the the symmetry-required degeneracy of two bands at the BZ boundary so that the two bands smoothly cross over into one another at the BZ boundary. Thus, although there are specific features of the FS of these compounds that reflect the symmetry of the crystal structure, there are no obvious features which reflect the chirality, a handedness or a left-right asymmetry, of this crystal structure which is thought to be responsible for the helimagnetism and the nucleation of skyrmion lattices in MnGe [36] and FeGe [19].

V. DISCUSSION AND CONCLUSIONS

We have synthesized and investigated the properties of cubic B20 MnGe, and CoGe as well as FeGe to explore the magnetic states of MnGe and to compare with the other B20

transition-metal monosilicides. CoGe is a small carrier density PM metal that is very similar to CoSi and is unremarkable in many respects. In contrast, the MnGe data presented here display many interesting features, particularly in the magnetic and thermodynamic properties. We summarize these results here and compare with the other HM *B*20 TM silicides and germanides in order to highlight how unusual the behavior of MnGe is. Our magnetic susceptibility data, both χ and χ' of our polycrystalline samples and the single crystal separated from the same sample growth, indicated a field-independent Curie-Weiss behavior above room temperature with a Weiss temperature of 270 K and a large fluctuating moment. This is consistent with the sharp peak in $\chi'(H=0)$ at 275 K indicating the formation of a magnetic state. This peak along with a small contribution to χ'' between 50 and 275 K are suppressed by magnetic fields of order 1 kOe. χ' evolves with field first into a steplike feature at lower temperature, and then to broad maximum above the field necessary to produce a field-polarized state. These features are similar to those discovered in the region of the *A* phase in FeGe and MnSi. In FeGe and MnSi, a peak associated with the Curie temperature evolves into a stepwise increase in χ' at a temperature that decreases with field, accompanied by a broad peak just above the zero field T_c and then, at higher H, to a simple broad peak whose maximum moves to higher temperature [33,38]. However, these features in MnSi and FeGe reside within a few K of T_c, whereas we observe a very wide T range where they evolve in MnGe. In addition, a broad peak at 180 K is apparent in MnGe that is suppressed by fields of order 10 kOe that has no counterpart in either MnSi or FeGe.

In addition to the features noted above, a sharp peak in χ' appears in MnGe below 150 K for fields greater than 5 kOe. This sharp signature moves to significantly lower temperatures with the application of larger fields and is clearly associated with a dramatic change in the magnetization curves below 150 K. At these temperatures, a broad region intermediate between the low-field HM state and a field-induced FM state emerges. The peaks in $\chi'(T,H)$ are accompanied by an equally sharp, first-order-like peak in $C_P(T)$ which originates at $H=0$ near 160 K where two peaks are apparent. These are in addition to a seemingly unrelated, field-independent peak at 119 K.

All of the features mentioned in the previous paragraphs are either absent in MnSi and FeGe or are, perhaps, present in the complex behavior in close proximity to T_c. It is well known that the behavior of MnSi and FeGe near the Curie point are characterized by a rich phase diagram which includes a HM low-field state that evolves with field to a conical state and finally a field-induced FM state. In addition, in a limited region of a few K below T_c over a field range of 1 to 2 kOe, the *A* phase, where a skyrmion lattice has been shown to arise, produces several features in χ', χ'', and C_P. For the most part, the specific heat of MnSi and FeGe are much simpler than the complex behavior we find in MnGe, displaying a single peak near T_c which is broadened by field and having subtle shoulders that are thought to indicate the so-called intermediate region just above T_c. This region is thus far poorly understood and has been suggested to host a glassy skyrmion phase [20]. Thus, our data indicate that MnGe may be either more complex than the better-known and -studied MnSi and FeGe, or that the *A* phase and perhaps the glassy skyrmion phase may exist in MnGe
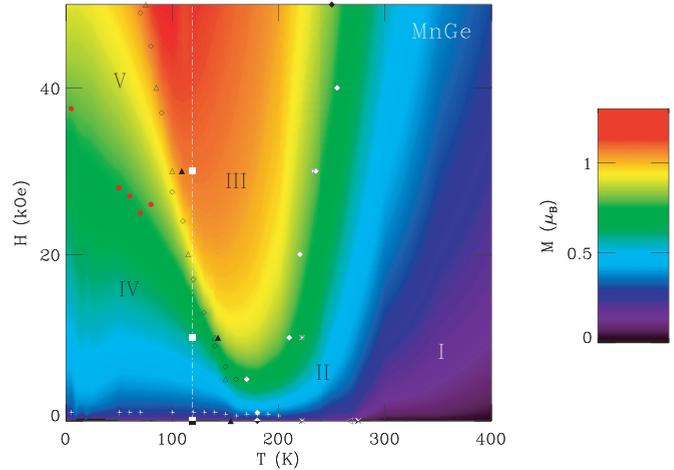

FIG. 23. (Color) Magnetic phase diagram: Contour plot of the magnetization M vs temperature T and field H. Symbols represent phase transitions or crossover behavior indicated in the data. Features observed in the specific heat (C) in Fig. 11 included are the H-independent phase transition (filled squares), the H-dependent phase transition (black filled triangles), the broad maximum observed near 225 K (asterisks), and the peak near the Curie T (left-pointing triangle). Features apparent in the T dependence of the ac susceptibility χ' (Fig. 4) include the Curie T (x), the sharp peaks apparent at finite field at $T < 150$ K (open triangles), and the broad maxima at $T > 150$ K (white and black diamonds). Maxima apparent in dM/dH determined from the data in Fig. 5 are shown as open diamonds and red bullets. Also observed in Fig. 5 is a region of large dM/dH at low fields at low H's (+). Roman numerals denote regions between these features for identification purposes.

that are somehow more apparent and cover a much wider field and temperature range.

The small-angle neutron scattering investigation of Kanazawa *et al.* [24] has already provided an indication that the latter may be true. These data on polycrystalline samples grown in a manner similar to our own indicate a transition to a HM-like state below 170 K with a HM wave vector that is larger than either FeGe or MnSi and that increases with decreased T. The changes that they observe with field and temperature lead the authors to conclude that the skyrmion lattice state not only exists over a much wider T and H than in MnSi and FeGe, but that it may be the ground state of the system, that is, existing at zero temperature and field. However, these impressive data do not indicate a cause for the phase transitions we observe in the specific heat nor the subtle magnetic state indicated in our χ' data between 165 and 275 K. The realization that the skyrmion lattice is much more stable in MnGe suggests that the phase transitions that we observe in χ' and $C_P(T,H)$ may very well be related to a symmetry change either within the skyrmion lattice state, or with the collapse of the skyrmion state as the system transitions to a more standard magnetic state such as a conical or a field-induced FM state.

We summarize what we have learned about the magnetic phase diagram of MnGe in Fig. 23 where we plot the magnetization in a contour plot. We have included benchmarks for the transitions we observe with with symbols denoting maxima in χ' and dM/dH as well as the peaks identified

in C_P. The phases denoted include region I, the high-T PM phase from which we have deduced a fluctuating moment of 1.35 μ_B/f.u. and a Weiss T of 275 K. Region II is the ill-defined magnetic state that occurs below $T_c = 275$ K that displays a transition to a field-induced FM state at higher fields (above 15 kOe at 200 K, region III in the figure). We make this assignment based upon the sharp peak in χ' at low fields and the substantial $M(H)$ above 200 K. Region IV denotes the low-H, low-T phase that is identified in the neutron scattering experiments [24,35,36] as either a HM phase or a skyrmion lattice phase. A first-order phase transition as either T or H are increased is required to enter phases II or III from region IV. The field-induced FM phase is identified as region III. Region IV appears to have a very similar low-H behavior to region II despite there being two phase transitions (one field dependent and one field independent) separating these two phases. At $T < 100$ K, a broad maximum in dM/dH is observed near 30 kOe which is indicated by the red bullets. We note that the skyrmion phase identified in Ref. [36] becomes disordered in this field range so that its signature in the small-angle neutron scattering data is not apparent above these fields (region V). The filled squares indicate the phase transition that we have observed at 119 K.

The low-T phases (regions IV and V in Fig. 23) display substantial differences from the isostructural compounds FeGe and MnSi. As we pointed out above, a much larger field is required to saturate the magnetization in MnGe, consistent with a much smaller, T-dependent, helical wavelength [24]. MnSi and FeGe both display a hysteresis much like that shown in Fig. 5 for initial field sweep after zero-field cooling. In addition, in MnSi and FeGe there is no evidence, that we are aware of, for a distinct phase transition in specific-heat measurements at temperatures substantially below T_c at any field as we have observed in MnGe.

The transport properties of MnGe are similar in many ways to those of isostructural FeGe. In each case, a metallic $\rho(T)$ with a RRR of about 10 along with a small negative MR is found for T exceeding T_c that increases upon cooling to 100 K [31,44]. This negative MR has been ascribed to magnetic fluctuation scattering in MnSi and FeGe and we interpret the MR in MnGe in a similar manner [45]. In addition, at low T, a small positive MR is observed in FeGe and MnGe below 50 K and in MnSi at $T < 1$ K [44,45]. The origin of this positive MR has not been established but has been suggested to be of

a semiclassical origin because the H dependence is consistent with a H^2 behavior [45]. Below 10 K, a T^2 dependence of $\rho(T)$ is observed with a magnitude that is consistent with the electronic contribution to the specific heat (although there are likely contributions to C_p from magnons in this T range) and is similar in magnitude to that found in MnSi at ambient pressure [44,45].

In conclusion, we have explored the structural, magnetic, thermodynamic, and transport properties of MnGe and CoGe stabilized by synthesis at high pressure. We find in agreement with previous work that a simple cubic, $B20$, crystal structure is stabilized that is common among TM monosilicides and monogermanides [1]. Although CoGe is a simple low carrier density metal much like CoSi, MnGe is magnetic with a HM-like magnetization curve below a T_c of 275 K. It displays interesting phase transitions at lower temperatures that have not been observed in the isostructural compounds. In addition, MnGe requires a much larger field to saturate the magnetization below 150 K than is seen at higher T or in the other HM $B20$ silicides and germanides suggesting a stronger influence of the Dzyaloshinskii-Moriya interaction. The transport properties of MnGe are much like those observed in FeGe and MnSi. Our data point out the need for single crystals and for further neutron diffraction and small-angle neutron scattering experiments to determine the structure of the magnetic states that we have identified in MnGe [35,36], the least investigated of the TM monogermanide and monosilicide family that have yielded so many compelling discoveries.

[1] J. H. Wernick, G. K. Wertheim, and S. K. Sherwood, Mater. Res. Bull. **7**, 1431 (1972).

[2] Y. Ishikawa, K. Tajima, D. Bloch, and M. Roth, Solid State Commun. **19**, 525 (1976).

[3] Y. Ishikawa, G. Shirane, J. A. Tarvin, and M. Kohgi, Phys. Rev. B **16**, 4956 (1977).

[4] O. Delaire, K. Marty, M. B. Stone, P. R. C. Kent, M. S. Lucas, D. L. Abernathy, D. Mandrus, and B. C. Sales, Proc. Natl. Acad. Sci. USA **108**, 4725 (2011).

[5] V. Jaccarino, G. K. Wertheim, J. H. Wernick, L. R. Walker, and S. Arajs, Phys. Rev. **160**, 476 (1967).

[6] G. Aeppli and Z. Fisk, Comments Condens. Matter Phys. **16**, 155 (1992).

[7] Z. Schlesinger, Z. Fisk, H.-T. Zhang, M. B. Maple, J. F. DiTusa, and G. Aeppli, Phys. Rev. Lett. **71**, 1748 (1993).

[8] N. Manyala, Y. Sidis, J. F. DiTusa. G. Aeppli, D. P. Young, and Z. Fisk, Nature (London) **404**, 581 (2000).

[9] N. Manyala, Y. Sidis, J. F. DiTusa. G. Aeppli, D. P. Young, and Z. Fisk, Nat. Mater. **3**, 255 (2004).

[10] N. Manyala, J. F. DiTusa, G. Aeppli, and A. P. Ramirez, Nature (London) **454**, 976 (2008).

[11] J. Beille, J. Voiron, and M. Roth, Solid State Commun. **47**, 399 (1983).

[12] O. Nakanishi, A. Yanase, A. Hasegawa, and M. Kataoka, Solid State Commun. **35**, 995 (1980).

[13] B. Lebech, J. Bernhard, and T. Freltoft, J. Phys.: Condens. Matter **1**, 6105 (1989).

[14] C. Pfleiderer, S. R. Julian, and G. G. Lonzarich, Nature (London) **414**, 427 (2001).

[15] C. Pfleiderer, D. Reznik, L. Pintschovius, H. von Lohneysen, M. Garst, and A. Rosch, Nature (London) **427**, 227 (2004).

[16] C. Pfleiderer and A. Rosch, Nature (London) **465**, 880 (2010).

[17] S. Muhlbauer, B. Binz, F. Jonietz, C. Pfleiderer, A. Rosch, A. Neubauer, R. Georgii, and P. Boni, Science **323**, 915 (2009).

[18] X. Z. Yu, Y. Onose, N. Kanazawa, J. H. Park, J. H. Han, Y. Matsui, N. Nagaosa, and Y. Tokura, Nature (London) **465**, 901 (2010).

[19] X. Z. Yu, N. Kanazawa, Y. Onose, K. Kimoto, W. Z. Zhang, S. Ishiwata, Y. Matsui, and Y. Tokura, Nat. Mater. **10**, 106 (2011).

[20] A. Neubauer, C. Pfleiderer, B. Binz, A. Rosch, R. Ritz, P. G. Niklowitz, and P. Boni, Phys. Rev. Lett. **102**, 186602 (2009).

[21] W. Munzer, A. Neubauer, T. Adams, S. Muhlbauer, C. Franz, F. Jonietz, R. Georgii, P. Boni, B. Pedersen, M. Schmidt, A. Rosch, and C. Pfleiderer, Phys. Rev. B **81**, 041203 (2010).

[22] D. van der Marel, A. Damascelli, K. Schulte, and A. A. Menovsky, Physica B (Amsterdam) **244**, 138 (1998).

[23] H. Hohl, A. P. Ramirez, C. Goldmann, G. Ernst, and G. Bucher, J. Alloys Compd. **278**, 39 (1998).

[24] N. Kanazawa, Y. Onose, T. Arima, D. Okuyama, K. Ohoyama, S. Wakimoto, K. Kakurai, S. Ishiwata, and Y. Tokura, Phys. Rev. Lett. **106**, 156603 (2011).

[25] T. Sato and M. Sakata, J. Phys. Soc. Jpn. **52**, 1807 (1983).

[26] T. Sato, J. Kozu, K. Oshiden, T. Nemoto, E. Ohta, M. Sakata, T. Goto, and T. Sakakibara, J. Phys. Soc. Jpn. **57**, 639 (1988).

[27] M. Richardson, Acta Chem. Scan. **21**, 2305 (1967).

[28] H. Takizawa, T. Sato. T. Endo, and M. Shimada, J. Solid State Chem. **73**, 40 (1988).

[29] T. Sato, E. Ohta, and M. Sakata, J. Magn. Magn. Mater. **61**, 205 (1986).

[30] L. Lundgren, O. Beckman, V. Attia, S. P. Batttacherjee, and M. Richardson, Phys. Scr. **1**, 69 (1970).

[31] S. Yeo, S. Nakatsuji, A. D. Bianchi, P. Schlottmann, Z. Fisk, L. Balicas, P. A. Stampe, and R. J. Kennedy, Phys. Rev. Lett. **91**, 046401 (2003).

[32] H. Wilhelm, M. Baenitz, M. Schmidt, C. Naylor, R. Lortz, U. K. Rößler, A. A. Leonov, and A. N. Bogdanov, J. Phys.: Condens. Matter **24**, 294204 (2012).

[33] H. Wilhelm, M. Baenitz, M. Schmidt, U. K. Rößler, A. A. Leonov, and A. N. Bogdanov, Phys. Rev. Lett. **107**, 127203 (2011).

[34] V. I. Anisimov, R. Hlubina, M. A. Korotin, V. V. Mazurenko, T. M. Rice, A. O. Shorikov, and M. Sigrist, Phys. Rev. Lett. **89**, 257203 (2002).

[35] O. L. Makarova, A. V. Tsvyashchenko, G. Andre, F. Porcher, L. N. Fomicheva, N. Rey, and I. Mirebeau, Phys. Rev. B **85**, 205205 (2012).

[36] N. Kanazawa, J. H. Kim, D. S. Inosov, J. S. White, N. Egetenmeyer, J. L. Gavilano, S. Ishiwata, Y. Onose, T. Arima, B. Keimer, and Y. Tokura, Phys. Rev. B **86**, 134425 (2012).

[37] N. Kanazawa, Y. Onose, Y. Shiomi, S. Ishiwata, and Y. Tokura, Appl. Phys. Lett. **100**, 093902 (2012).

[38] A. Bauer, A. Neubauer, C. Franz, W. Munzer, M. Garst, and C. Pfleiderer, Phys. Rev. B **82**, 064404 (2010).

[39] U. K. Rößler, J. Phys.: Conf. Ser. **391**, 012104 (2012).

[40] A. Arrott and J. E. Noakes, Phys. Rev. Lett. **19**, 786 (1967).

[41] D. M. Edwards and E. P. Wohlfarth, Proc. R. Soc. A **303**, 127 (1968).

[42] See, e.g., N. W. Ashcroft and N. D. Mermin, *Solid State Physics* (Saunders, Philadelphia, 1976).

[43] K. Marklund, M. Larsson, S. Bystom, and T. Lindqvist, Phys. Scr. **9**, 47 (1974).

[44] C. Capan, J. F. DiTusa, A. B. Karki, D. P. Young, A. D. Bianchi, L. D. Pham, Z. Fisk, E. L. Thomas, J. Y. Chan, and G. Aeppli (to be published).

[45] K. Kadowaki, K. Okuda, and M. Date, J. Phys. Soc. Jpn. **51**, 2433 (1982).

[46] K. Kadowaki and S. B. Woods, Solid State Commun. **58**, 507 (1986).

[47] M. Lee, Y. Onose, Y. Tokura, and N. P. Ong, Phys. Rev. B **75**, 172403 (2007).

[48] P. Blaha, K. Schwarz, G. K. H. Madsen, D. Kvasnicka, and J. Luitz, WIEN2K, An Augmented Plane Wave + Local Orbitals Program for Calculating Crystal Properties (Karlheinz Schwarz, Techn. Universität Wien, Austria, 2001).

[49] J. P. Perdew, K. Burke, and M. Ernzerhof, Phys. Rev. Lett. **77**, 3865 (1996).

[50] P. E. Blöchl, O. Jepsen, and O. K. Andersen, Phys. Rev. B **49**, 16223 (1994).

[51] M. Deutsch, O. L. Makarova, T. C. Hansen, M. T. Fernandez-Diaz, V. A. Sidorov, A. V. Tsvyashchenko, L. N. Fomicheva, F. Porcher, S. Petit, K. Koepernik, U. K. Rößler, and I. Mirebeau, Phys. Rev. B **89**, 180407 (2014).

[52] H. Yamada, K. Terao, H. Ohta, and E. Kulatov, Physica B (Amsterdam) **329–333**, 1131 (2003).

[53] T. Jarlborg, J. Magn. Magn. Mater. **283**, 238 (2004).

[54] V. V. Mazurenko, A. O. Shorikov, A. V. Lukoyanov, K. Kharlov, E. Gorelov, A. I. Lichtenstein, and V. I. Anisimov, Phys. Rev. B **81**, 125131 (2010).

[55] Z. J. Pan, L. T. Zhang, and J. S. Wu, Comput. Mater. Sci. **39**, 752 (2007).

[56] T. Jeong and W. E. Pickett, Phys. Rev. B **70**, 075114 (2004).